LANGMUIR

Invited Feature Article

pubs.acs.org/Langmuir

Water-Mediated Interactions between Hydrophilic and Hydrophobic Surfaces

Matej Kanduč,*[,†] Alexander Schlaich,[‡] Emanuel Schneck,[§] and Roland R. Netz*[,‡]

[†]Soft Matter and Functional Materials, Helmholtz-Zentrum Berlin für Materialien und Energie, Hahn-Meitner-Platz 1, D-14109 Berlin, Germany

[‡]Department of Physics, Freie Universität Berlin, Arnimallee 14, D-14195 Berlin, Germany

[§]Max Planck Institute of Colloids and Interfaces, Am Mühlenberg 1, D-14476 Potsdam, Germany

Supporting Information

ABSTRACT: All surfaces in water experience at short separations hydration repulsion or hydrophobic attraction, depending on the surface polarity. These interactions dominate the more long-ranged electrostatic and van der Waals interactions and are ubiquitous in biological and colloidal systems. Despite their importance in all scenarios where the surface separation is in the nanometer range, the origin of these hydration interactions is still unclear. Using atomistic solvent-explicit molecular dynamics simulations, we analyze the interaction free energies of charge-neutral model surfaces with different elastic and water-binding properties. The surface polarity is shown to be the most important parameter that not only determines the hydration properties and thereby the water contact angle of a single surface but also the surface−surface interaction and whether two surfaces attract or repel. Elastic properties of the surfaces are less important. On the basis of surface contact angles and surface−surface binding affinities, we construct a universal interaction diagram featuring three different interaction regimes—hydration repulsion, cavitation-induced attraction—and for intermediate surface polarities—dry adhesion. On the basis of scaling arguments and perturbation theory, we establish simple combination rules that predict the interaction behavior for combinations of dissimilar surfaces.

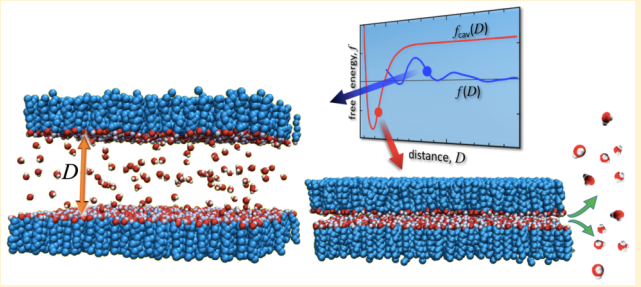

1. INTRODUCTION

The behavior of soft matter on the nanoscale is largely governed by the surface properties of its constituents. Surface interactions are decisive for the stability of colloidal suspensions or foams and more generally for the structural organization of complex fluids.[1] Apart from its technological relevance, this aspect is of particular importance for all biological matter, where extended molecular layers are major components, for instance, in the form of biomembranes.[2] Membrane−membrane and membrane−surface interactions affect cell adhesion,[3] the mechanical properties of bacterial biofilms,[4] biomineral formation,[5] and the adsorption of organisms to natural and man-made materials.[6] The characteristics of surface interactions in an aqueous environment, such as interaction strength and range, as well as whether interactions are repulsive or attractive in general depend on the chemical composition of the surfaces involved. The interaction of biomembranes, for example, is sensitive to the relative fractions of neutral and charged lipid headgroups on their surfaces and to the presence of membrane-bound saccharides, polypeptides, and macromolecules.[7] Similarly, interfacial forces between particles in technologically relevant colloidal suspensions are determined by their surface chemistry. For example, hydrophobic particles, which normally aggregate in water, remain separated when their surfaces are functionalized with amphiphilic molecules. In summary, surface interactions in aqueous environments are of great importance in biology and from a technological viewpoint. Comprehensive knowledge of the underlying physical mechanisms is thus a prerequisite to understanding numerous biological processes as well as for the rational design of surfaces exhibiting desired interaction characteristics. Technological applications include cell-sorting devices,[8] lubricants,[9] and programmable and self-cleaning surfaces.[10]

The interaction between two surfaces in an aqueous environment in general involves the interplay of various interfacial forces, including among others electrostatic forces, van der Waals (vdW) forces, and solvation and steric forces,[11] rendering a quantitative description very difficult, especially for surfaces of complex chemical composition. To shed light on the interaction mechanisms in a systematic manner, the focus of research has moved toward well-defined surfaces with rather simple chemical composition[12−14] or even idealized (structureless) surfaces.[15−17] In fact, even the interaction between such simplified surfaces is understood only partially. When they are electrically neutral, their interaction at small separations is dominated by solvation forces such as hydration repulsion and

Received: May 6, 2016
Revised: July 26, 2016
Published: August 3, 2016

DOI: 10.1021/acs.langmuir.6b01727
Langmuir 2016, 32, 8767−8782

hydrophobic attraction. On one end of the spectrum are hydrophilic surfaces, such as mica, which possess polar groups in high densities that are capable of forming hydrogen bonds with water molecules. These surfaces are characterized by small or even vanishing water contact angles. Upon bringing two hydrophilic interfaces together, removing the hydration water causes a strong, repulsive hydration pressure.[18−21] Hydration repulsion universally acts between sufficiently polar hydrated surfaces even when they are overall charge neutral and typically decays exponentially with distance, with a characteristic decay length of a fraction of a nanometer.[18,21,22] At nanometer separations, hydration repulsion typically overshadows all other surface interactions, such as electric double layer, van der Waals, and undulation forces.[12,23,24] On the other end of the spectrum are nonpolar, hydrophobic surfaces, such as polystyrene and alkane-functionalized surfaces. They are characterized by contact angles $\theta > 90°$. The hydrogen-bonding network of water is distorted at such surfaces because they do not form hydrogen bonds. This results in a fluctuating vapor−water-like depletion layer at the surface with far-reaching consequences for solvation processes and self-assembly.[25−30] As two hydrophobic surfaces approach each other, liquid interlamellar water becomes metastable with respect to the vapor phase at a threshold surface separation, and a drying transition expels the water into the bulk, leaving a vapor cavity between the surfaces.[15,31−34] The water cavitation induces long-range attraction between the surfaces. However, because of the high free-energy barriers associated with the drying transition,[35−38] the interlamellar water can persist in a metastable state down to several nanometers of separation before the drying transition actually occurs.[12,39,40] In fact, a large fraction of the literature on hydrophobic attraction is concerned with secondary effects such as contamination, bridging nanobubbles, surface instabilities, deformations, and monolayer folding as well as kinetic effects, which, taken together, make the experimental measurement of hydrophobic interactions inherently difficult.[12,39−42]

The drying or cavitation transition occurs only between hydrophobic surfaces, with contact angles of $\theta > 90°$. Nevertheless, a number of studies reported attraction even between hydrophilic surfaces with contact angles as low as 65°,[6,43−46] which could not be rationalized by van der Waals attraction. Various experiments reported force measurements between symmetric self-assembled monolayers with contact angles tuned by regulating the proportion of polar and nonpolar surface groups.[43,45,46] In other experiments, the adsorption of proteins[6] and single peptide chains[47] or the settlement of various algae[6] on substrates with controllable contact angles was investigated. Quite universally, surfaces possess adhesive properties for contact angles above a critical value, which is found to be around $\theta_{adh} \approx 60−80°$[44] and thus substantially smaller than 90°.

A more intricate picture emerges for asymmetric scenarios, where the interacting surfaces exhibit different contact angles. A number of experimental model studies addressed the interactions between dissimilar surfaces and the particularly interesting case of a hydrophobic surface interacting with a hydrophilic one.[12−14,41,48−50]

The understanding of hydration and hydrophobic surface interactions has recently been advanced by insights from computer simulations that include explicit water molecules.[15,16,38,51−54] Here, a particular challenge is the control of the chemical potential of water between the interacting surfaces.[55] Namely, one has to consider that water is in chemical equilibrium with an external bulk reservoir, allowing for the exchange of water molecules as the surface separation changes. Several techniques to prescribe the water chemical potential in simulations have been established,[56] such as an explicit water reservoir[51,53,57−61] or grand canonical Monte Carlo approaches.[15,62,63] During the last couple of years, we have established a versatile and accurate method, termed thermodynamic extrapolation (TE), to account for the water chemical potential in solvent-explicit molecular dynamics simulations with realistic representations of all sorts of interacting surfaces.[64,65] Using this technique, we recently addressed the crossover from hydration repulsion to adhesion between similar[65] and dissimilar pairs of surfaces.[66] We found that the adhesion transition crucially depends on the interplay between direct surface interactions and the water binding affinity to the surfaces, which is reflected in the contact angle.[65]

In the present work, we generalize our findings for a broader range of surface types. In particular, we scrutinize the influence of the surfaces' capability to form intra- and intersurface hydrogen bonds. After analyzing the symmetric scenario of interacting identical surfaces, we proceed with the asymmetric case, where we derive combination rules for interactions between dissimilar surfaces. At the end, we briefly discuss finite-size effects and the effect of chemical heterogeneities, which are important for most biological and many technologically relevant surfaces.

2. COMPUTER MODELS OF INTERACTING SURFACES

To systematically study water-mediated interactions, we utilize simple atomistic model surfaces mimicking self-assembled monolayers (SAMs), introduced in our previous work.[65] Here, two parallel planar surfaces are each composed of 100 alkane chains terminated by hydroxyl (OH) headgroups facing the water phase in the middle (Figure 1). The simulation box has lateral dimensions of 5.2 nm × 4.5 nm and is repeated in all three directions via periodic boundary conditions so that an infinite stack of layers is mimicked. The layers are stabilized by anchor potentials acting on a set of selected atoms listed in

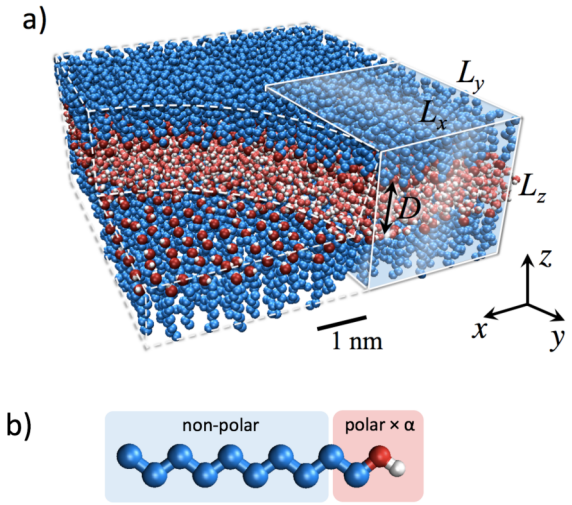

Figure 1. (a) Simulation snapshot of two stiff surfaces (type I) interacting across a water layer. The simulation box with dimensions of $L_x \times L_y \times L_z$, indicated by a white frame, is replicated in all three directions via periodic boundary conditions. (b) A surface molecule is composed of an alkane chain terminated by a modified hydroxyl group whose polarity is rescaled by a factor α.

DOI: 10.1021/acs.langmuir.6b01727
Langmuir 2016, 32, 8767−8782

Table 1. Further simulation details are described in the Supporting Information. To evaluate the properties of the

Table 1. Summary of the Surface Model Parameters[a]

	anchors	headgroup repulsion
type I	stiff	large
type II	intermediate	large
type III	intermediate	intermediate
type IV	soft	large
type V	soft	small
type VI	intermediate	small
Anchors:		
stiff	$k_x = k_y = 500$, $k_z = 1000$	H, C_1, C_2, C_9, C_{10}
intermediate	$k_x = k_y = 500$, $k_z = 1000$	C_1, C_2, C_9, C_{10}
soft	$k_x = k_y = 500$, $k_z = 10$	C_2
Headgroup Repulsion:		
large	$C_{12} = 10 \times 10^{-6}$ nm^{12} kJ/mol	($\sigma = 0.40$ nm)
intermediate	$C_{12} = 3.5 \times 10^{-6}$ nm^{12} kJ/mol	($\sigma = 0.34$ nm)
small	$C_{12} = 1.5 \times 10^{-6}$ nm^{12} kJ/mol	($\sigma = 0.30$ nm)

[a]Harmonic anchor potentials with specified spring constants k_x, k_y, and k_z, given in units of kJ/mol/nm^2, act on selected surface atoms listed in the right column. The index on a C atom labels its successive position counted from the OH group. The repulsion between headgroups is controlled by modifying the repulsive C_{12} coefficient of LJ interaction between the headgroup oxygens. The corresponding effective LJ diameter of the headgroup, $\sigma = (C_{12}/C_6)^{1/6}$, is shown in parentheses. The smallest value ($\sigma = 0.30$ nm) corresponds to the unmodified GROMOS force field.[67]

system at prescribed chemical potential, we utilize the TE technique[64,65] in which the number of water molecules confined between the surfaces is kept constant so that the chemical potential of water typically deviates from the reference bulk value. Via the precise determination of the water chemical potential between the surfaces and its deviation from the reference value in bulk water, the number of water molecules and the interaction pressure that corresponds to the prescribed chemical potential can be computed. The details of the method are described in the Supporting Information.

We focus on three different model parameters with which we control the general properties of the surfaces. The first and most important parameter that controls the wetting properties is the surface polarity. Varying this parameter allows us to study the influence of the chemical composition in a generic manner. In our model, we modify the headgroup dipole moments by rescaling the partial charges of hydroxyl groups by a dimensionless polarity parameter α, which ranges from 0 to 1. The case of $\alpha = 1$ corresponds to a completely polar surface with actual hydroxyl headgroups characterized by full partial charges, whereas the other extreme with $\alpha = 0$ corresponds to the completely nonpolar scenario with headgroups resembling methylated termini.

The second tunable property is the mechanical stiffness of the layers, which is an important aspect for the interaction of "soft" interfaces, often found in biology and wet technology. In our model, the stiffness is controlled by adjusting the strengths of the anchor potentials. For very strong anchors, the surfaces become crystalline-like, whereas softer variants with thermally mobile groups correspond to soft SAMs or fluid membranes (e.g., lipid bilayers).

The third adjustable characteristic is the ability of headgroups to form hydrogen bonds (HBs) between themselves. Under experimental conditions, this ability depends on the lattice parameters for solid surfaces and on the molecular geometry and packing density for surfaces of self-assembled amphiphilic layers. Note that in our model the headgroups are arranged on a perfect hexagonal lattice in a plane, which allows for unrealistically high HB formation between the headgroups within a monolayer. Therefore, we also analyze scenarios with suppressed intra- and intersurface hydrogen-bonding capability. This we achieve by increasing the repulsive coefficient in the Lennard-Jones (LJ) interaction between oxygen atoms in the OH headgroups, as discussed further below.

By considering several different stiffnesses along with several different HB capabilities, we set up six different surface types that we study, as summarized in Table 1. For each surface type, we consider the full range of surface polarities α, from completely nonpolar to completely polar situations.

3. SYMMETRIC SCENARIO

The most important thermodynamic quantity that determines the hydration properties of a surface is the wetting coefficient, defined as

$$k_w = \frac{\gamma_{sv} - \gamma_{sw}}{\gamma} \tag{1}$$

where γ_{sv}, γ_{sw}, and γ are surface−vapor, surface−water, and water−vapor surface tensions, respectively. The wetting coefficient reflects the water binding affinity to the surface and is via Young's equation related to the contact angle θ as

$$\cos\theta = \begin{cases} k_w & \text{for } k_w \le 1 \\ 1 & \text{for } k_w > 1 \end{cases} \tag{2}$$

In the case of $k_w > 1$, corresponding to $\theta = 0°$, one speaks of complete wetting, where a water droplet spreads entirely over the surface. Note that a surface in contact with vapor typically forms a thin liquid film, which modifies the surface−vapor surface tension γ_{sv}. Strictly speaking, one distinguishes between "dry" and "moist" surface tensions, depending on whether the surface is in vacuum or in equilibrium with a vapor phase.[68−70] If the amount of adsorbed water in the film is large, then it alters the wetting coefficient and the contact angle. The liquid film formation for these kinds of surfaces has been analyzed theoretically in ref 66, and it was shown that it becomes important only for polarities close to the transition of complete wetting. For simplicity, we will in this work neglect the film formation and consider the "dry" variants of k_w and θ.

The wetting coefficient is a measure of the free energy of water cavitation. The work per surface area A needed to expel the water located between two identical surfaces at large separation into the water reservoir is equal to

$$f_{vac}(D \to \infty) = 2(\gamma_{sv} - \gamma_{sw}) = 2\gamma k_w \tag{3}$$

Here we have neglected edge effects and the work contribution due to atmospheric pressure, which we discuss in more detail in section 5.1. The result in eq 3 implies that for hydrophobic surfaces characterized by $k_w < 0$, or equivalently by $\theta > 90°$, the work becomes negative and thus the water slab spontaneously retreats into the bulk, leaving the vapor phase behind. At thermodynamic equilibrium, only hydrophilic surfaces (i.e., surfaces characterized by $\theta < 90°$) remain hydrated down to

DOI: 10.1021/acs.langmuir.6b01727
Langmuir 2016, 32, 8767−8782

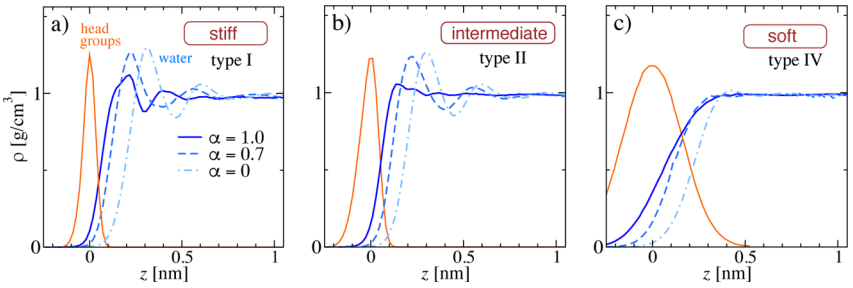

Figure 2. Density profiles of water (blue curves) at surfaces with different polarities α ranging from (a) stiff to (c) soft. The headgroup oxygen density profiles for the $\alpha = 1$ case, shown by orange bell-shaped curves, are scaled such that their peaks have the same height. The headgroup-oxygen density profiles for $\alpha = 0.7$ and 0 are almost indistinguishable from the $\alpha = 1$ case and are hence not shown. In these simulations, the second surface is placed sufficiently far away, at a separation of $D > 2$ nm, such that it does not influence the density profiles.

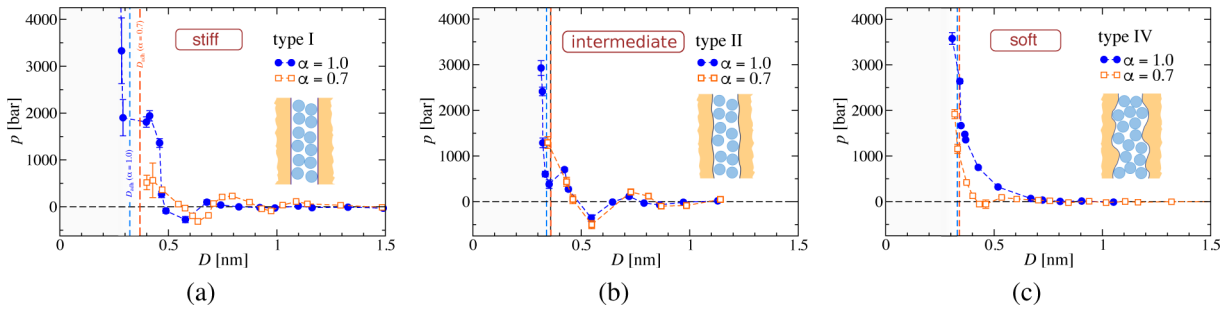

Figure 3. Hydration pressures between identical surfaces with polarities of $\alpha = 1$ and 0.7 for (a) surface type I (stiff), (b) surface type II (intermediate), and (c) surface type IV (soft). The vertical dashed lines indicate the close-contact distance D_{adh}. Insets schematically illustrate water layering at a distance of around $D \approx 0.8$ nm, where two water layers are present.

small separations. Therefore, it only makes sense to analyze the equilibrium hydration behavior of hydrophilic surfaces, which first requires a determination of the wetting coefficients. In our simulations, we evaluate the wetting coefficient by the thermodynamic integration (TI) method, which allows us to determine contact angles with a precision of 2 to 3°, as described in the Supporting Information.

3.1. Influence of Surface Stiffness. We start with a short discussion of the influence of the surface stiffness on the interfacial water behavior and the hydration pressure acting in the z direction between the surfaces. In Figure 2, we take a look at surface types I, II, and IV whose molecules do not form significant hydrogen bonds between themselves; that is, they have low surface−surface HB capabilty. The influence of the latter will be discussed in the next section. In surface type I, we strongly restrain the alkane chains as well as the hydrogen atoms in the headgroups. By releasing the hydrogen atoms, we obtain surface type II. In surface type IV, the chains are only minimally restrained and the surface headgroups can fluctuate considerably as indicated by the headgroup oxygen density distributions shown in orange.

Figure 2 shows water density profiles at the three surfaces. At the stiffest surface of type I, water molecules tend to order in distinct layers, which leads to oscillations in the density profiles. Layering becomes more pronounced at less polar stiff surfaces, as can be deduced from the comparison of type I surfaces for different values of polarity parameter α in Figure 2a. Note that in general increased polarity can both enhance[71,72] or suppress[65,73] water layering, depending on the complex interplay of water and surface molecular interactions. Apart from the density oscillations, the depletion zone between the headgroups and water also grows with decreasing polarity (Figure 2). This reflects the affinity with which water is bound to the surface, as has been demonstrated previously.[26,28,71] Upon a slight decrease in surface stiffness (cf. Figure 2a,b), the layering decreases for the highest polarity, whereas it barely changes for lower polarities. In the case of the soft surfaces in Figure 2c, where the headgroup undulations exceed the size of a water molecule, the layering is smeared out and the water density profiles decay monotonically to zero on the length scale of the headgroup fluctuations.

Water layering profoundly affects the hydration pressure when two surfaces are brought together to small separations. Figure 3 shows the interaction pressures acting in the normal direction between identical surfaces of high ($\alpha = 1$) and moderate polarities ($\alpha = 0.7$). For all surface types in Figure 3, the pressure reaches thousands of bars at close contact and decays with increasing surface separation D. In this work, the separation D between surfaces is defined as the distance between the oxygen atoms on the opposing surfaces (Figure 1a). The vertical dashed lines in Figure 3 represent the close-contact distance D_{adh} that corresponds to the equilibrium distance of the surfaces in vacuum, as will be discussed in more detail further below. A fundamental difference between the soft and stiff surfaces appears as a result of water layering, which induces oscillations in the pressure−distance curves. Each oscillation in the pressure corresponds to the expulsion of exactly one water layer from the interlamellar region.[65] In the Supporting Information, we show that the periods of density and pressure oscillations match. The oscillatory nature of the interaction, which has been observed experimentally for very flat crystalline surfaces,[20] is hence a structural effect of the solvent. On the other hand, if the interfacial water does not exhibit layering, then the pressure decays almost monotonically with distance, as is the case for the soft surfaces in Figure 3c. The monotonic decay is hence typical for soft interfaces, such as lipid membranes.[18,74]

DOI: 10.1021/acs.langmuir.6b01727
Langmuir 2016, 32, 8767−8782

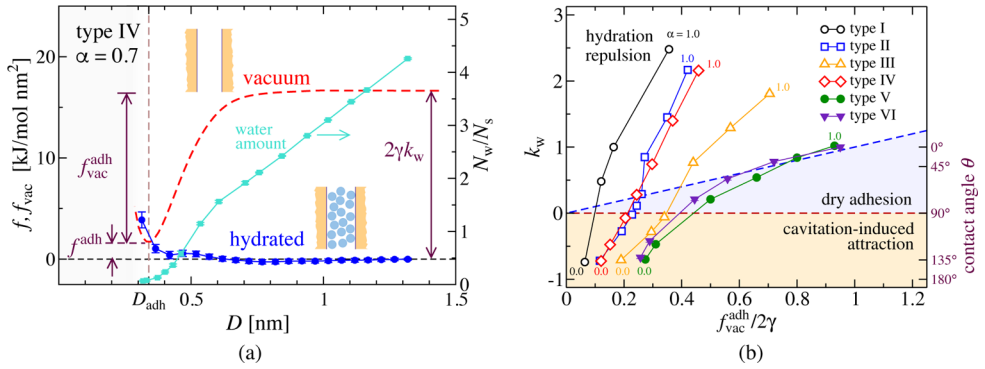

Figure 4. (a) Free energy profiles for soft type IV surfaces in the hydrated and vacuum states. The amount of interlamellar water in the hydrated state is shown by turquoise data points with the scale on the right. In the close-contact state at $D = D_{adh}$, indicated by a vertical dashed line, almost all interlamellar water is expelled and the free energies of hydrated and cavitated states coincide. (b) Interaction diagram in terms of the surface wetting coefficient k_w (with corresponding contact angle θ on the right) versus the rescaled work of adhesion in vacuum $f_{vac}^{adh}/2\gamma$, exhibiting three distinct interaction regimes. Explicit simulation results for the six surface types with polarity ranging from $\alpha = 0$ to 1.0 are denoted by symbols that are connected by lines.

However, because of a complex interplay of various antagonistic interaction mechanisms, weak nonmonotonies can also emerge.

For lower polarities α, the surfaces eventually become hydrophobic and the water film exhibits cavitation as discussed above. To account for the possibility of cavitation, we have to compare the distance-resolved free energies of the cavitated and hydrated states. The free energy per surface area of the hydrated system follows by integrating the interaction pressure over distance D,

$$f(D) = \int_D^\infty p(D')\frac{dL_z(D')}{dD'}\,dD' \tag{4}$$

Here, the differential factor $dL_z(D')/dD'$ of the repeat distance L_z (Figure 1a) includes the contribution of surface deformation at higher pressures, which is significant for softer surfaces. By this definition, the free energy of the hydrated state is zero at large separations, $f(D \to \infty) = 0$. Similarly, the free energy of the cavitated state follows from the integration of the pressure p_{vac} acting between the surfaces across vacuum (or vapor), namely,

$$f_{vac}(D) = 2\gamma k_w + \int_D^\infty p_{vac}(D')\frac{dL_z(D')}{dD'}\,dD' \tag{5}$$

Here, the constant term $2\gamma k_w$ accounts for the interfacial work of expelling the interlamellar water between the surfaces at large distances into the bulk, as given in eq 3. As a generic example, we show the free energies for type IV surfaces with polarity $\alpha = 0.7$ and a corresponding contact angle of $\theta = 75°$ in Figure 4a. The free energy $f(D)$ of the hydrated state, shown by a blue curve, starts from zero at large separations D and rises as the surfaces come together, reflecting hydration repulsion between the surfaces. The amount of interlamellar water in the hydrated state is shown by a turquoise curve, with the scale on the right side of the diagram. As expected, the amount of water decreases as the surfaces approach each other. The functional dependence is not linear, which reflects surface compressibility and nonideal water mixing effects, as will be discussed further in section 3.2. On the other hand, the free energy of the cavitated state $f_{vac}(D)$, represented by a red dashed line, starts at $2\gamma k_w = 2\gamma \cos\theta$ at large separations. Because, in this case, for sufficiently large separation the hydrated state has lower free energy, $f(D) < f_{vac}(D)$, the surfaces are hydrated in thermodynamic equilibrium. Upon approach of the surfaces, the free energy of the cavitated state decreases as a result of attractive forces acting between the surfaces in vacuum. In the close-contact state at $D = D_{adh}$ where the attractive forces are counteracted by steric repulsion between the surface atoms, the free energy reaches a minimum with a depth of f_{vac}^{adh}. The value f_{vac}^{adh} hence corresponds to the vacuum adhesion energy, that is, the work needed to separate the surfaces across a vacuum (cf. Figure 4a). Within the numerical accuracy, for the close-contact distance, $D = D_{adh}$, the free energies of both states meet at the value of the adhesive free energy, that is, $f^{adh} \equiv f_{vac}(D_{adh}) \simeq f(D_{adh})$. In the hydrated state at this distance, almost all of the water has been expelled into the bulk water reservoir, and thus $N_w \approx 0$. Consequently, the hydrated state and the cavitated state become indistinguishable and their free energies assume the same values. This means that the free energy of the close-contact state can be expressed in terms of the wetting coefficient k_w and the adhesion free energy in vacuum f_{vac}^{adh} as

$$f^{adh} = 2\gamma k_w - f_{vac}^{adh} \tag{6}$$

Due to entropic effects, N_w can never reach strictly zero in the hydrated state, which is especially relevant for highly polar surfaces that have a strong binding affinity for water. In the latter case, the free energies of the cavitated and hydrated states do not meet exactly at D_{adh} but at a slightly lower separation, as is shown in Figure 7b. For separations of $D < D_{adh}$, both curves increase dramatically as a result of the elastic penalty of surface compression.

As seen in Figure 4a, the free energy of the hydrated state exhibits a very shallow minimum at around $D \approx 0.8$ nm, which we associate with a combination of van der Waals (vdW) and more complex water-mediated interactions between the surfaces.[66] We also observe similar hydrated free energy minima for other surface combinations, with depths typically of less than 1 kJ/mol/nm^2.[66] In the literature on interacting amphiphilic layers, most prominently on lipid bilayers, a weakly bound hydrated state has been commonly reported and successfully described in terms of a balance between short-ranged repulsive (hydration) forces and an attractive vdW force of longer range.[74−76] The vdW attraction between media with different dielectric properties is also represented in the simulations via the LJ potentials acting between all atom pairs. However, because of a cutoff in the LJ potentials at 0.9 nm, the long-range behavior of the vdW attraction is not described correctly.[77] Moreover, these shallow wet adhesive states are much weaker than the typical

DOI: 10.1021/acs.langmuir.6b01727
Langmuir 2016, 32, 8767−8782

hydration and cavitation energies of tens to hundreds of kJ/mol/nm^2 that we are dealing with in the present work. Therefore, in the following text, we disregard wet adhesive states from the discussion and do not distinguish between such states and the states corresponding to infinite hydration. With this simplifying assumption, the global free energy minimum is either the hydrated state at large separations $D \to \infty$ or the dry adhesive state at close contact D_{adh}, defined via the minimum in $f_{vac}(D)$.

It is instructive to examine different surfaces and categorize them in an interaction diagram in terms of k_w versus $f_{vac}^{adh}/2\gamma$, as shown in Figure 4b. For $k_w < 0$ (i.e., for $\theta > 90°$), shown by the orange shaded region, the surfaces are hydrophobic and subject to long-ranged cavitation-induced attraction, regardless of the vacuum adhesion free energy f_{vac}^{adh}. On the other hand, for $k_w > 0$ the surfaces are hydrophilic, with $\theta < 90°$, and remain hydrated down to the close-contact state. Whether the surfaces attract ($f^{adh} < 0$) or repel ($f^{adh} > 0$) in the close-contact state depends on the competition between direct surface−surface attraction, characterized by f_{vac}^{adh}, and the water binding affinity to the surface, described by k_w. For very polar surfaces, we have $k_w > f_{vac}^{adh}/2\gamma$, and according to eq 6, the adhesive free energy f^{adh} is positive and the surfaces repel via hydration repulsion, as shown by a white region in the diagram. The hydration repulsion reflects the work required to remove strongly bound water molecules from the surfaces. If, on the other hand, $k_w < f_{vac}^{adh}/2\gamma$, as represented by the blue shaded region, then the close-contact state has lower free energy than when the hydrated surfaces are far apart. In such a case, hydrophilic surfaces globally attract at short distances. By coming into close contact, all of the water is expelled into the bulk, which we denote as dry adhesion.

Very generally, all completely nonpolar surfaces lie deeply in the cavitation-induced attraction region of the diagram. With increasing polarity α, we move upward in the diagram, cross the universal cavitation threshold at $\theta = 90°$, pass the dry-adhesion region, and eventually enter the hydration repulsion regime for large-enough polarities. Aforementioned surface types I, II, and IV, which all have low surface−surface HB capability, show very similar behavior with increasing polarity. In particular, surfaces of type II and IV, as well as V and VI, which differ only in the elastic surface properties, lie very close to each other in the interaction diagram. In other words, surface elasticity changes the shape of the pressure profiles, as seen in Figure 3, but does not change the adhesive surface properties as much, as seen in the interaction diagram in Figure 4b.

3.2. Hydration-Dependent Partial Water Volume. An important observable, which is also accessible in experiments, is the amount of interlamellar water between the surfaces and its change upon variation of the surface separation. This quantity drastically depends on the thermodynamic boundary conditions. When surfaces are in contact with a water reservoir, as is the case in our study, the chemical potential of the interlamellar water is fixed. In this case, the amount of interlamellar water N_w is dictated by the change in the system volume V. The corresponding response function v_μ, defined as

$$v_\mu^{-1} = \left(\frac{\partial N_w}{\partial V}\right)_\mu \tag{7}$$

is the partial water volume at constant chemical potential. It represents the required change in the system volume at fixed chemical potential in order to expel one water molecule from the interlamellar region. In Figure 5, we show v_μ as a function of the surface separation for soft polar surfaces as red squares. At large surface separations, where the interaction pressure is negligible, v_μ approaches the volume of an SPC/E water molecule in bulk $V/N_w = v_0 = 0.030$ nm^3. At small separations, substantial pressures are required to expel water molecules, as seen in Figure 3c. These high pressures also compress the soft alkane chains, which significantly contributes to the overall change in the system volume, and v_μ increases dramatically as $D \to D_{adh}$ and reaches a value of $v_\mu \approx 0.1$ nm^3 for the smallest separations. Note that the separation D for very high pressures becomes smaller than D_{adh} as a result of surface compression, meaning that the oxygens on opposing surfaces approach more than in the adhesive case in vacuum.

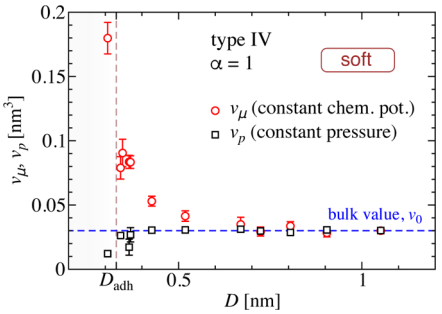

Figure 5. Partial water volumes at constant chemical potential (v_μ) and at constant pressure (v_p) as a function of the separation between soft polar surfaces of type IV. The vertical dashed line denotes the close-contact separation D_{adh}, and the horizontal dashed line indicates the bulk water volume, v_0.

Alternatively, the interacting surfaces can be held at constant pressure, a scenario relevant for example in osmotic stress experiments at atmospheric pressure.[78] In this case, the change in N_w occurs at constant pressure with varying water chemical potential. The corresponding response of the system volume can be expressed in terms of the partial water volume at constant pressure,

$$v_p = \left(\frac{\partial V}{\partial N_w}\right)_p \tag{8}$$

Black squares in Figure 5 indicate v_p for soft polar surfaces and its dependence on the surface separation. In contrast to v_μ, v_p remains approximately constant and equal to v_0 down to the lowest hydration levels. The moderate decrease in v_p near the close-contact state ($D \to D_{adh}$) suggests that the removal of the last water molecules leaves voids between the opposing surfaces and the system volume accordingly decreases by less than v_0. The partial volumes, v_μ and v_p, play an important role in determining the pressure at a prescribed chemical potential via our thermodynamic extrapolation technique, as explained in the Supporting Information. They also demonstrate the complex coupling between surface hydration and the thermodynamic ensemble.

The variation of v_p with distance has to be considered when interpreting results from osmotic stress experiments. There, the so-called equivalent interaction pressure is calculated from the shift $\mu - \mu_0$ of the water chemical potential from the bulk reference value, $p = -(\mu - \mu_0)/v_p$. If v_p decreases at small distances, as in Figure 5, then the equivalent pressure is actually higher than if assuming constant $v_p = v_0$. The latter assumption is commonly made in experiments and is often an acceptable approximation. However, the experimental determination of v_p

DOI: 10.1021/acs.langmuir.6b01727
Langmuir 2016, 32, 8767−8782

would be desirable not only for validating the calculation of the equivalent pressure but also for a critical comparison with the respective value obtained in computer simulations.

To establish a thermodynamic relation between v_μ and v_p, we describe the system volume as a state function $V(N_w, p)$ (disregarding T, which is constant) with the total differential

$$dV = \left(\frac{\partial V}{\partial N_w}\right)_p dN_w + \left(\frac{\partial V}{\partial p}\right)_{N_w} dp \tag{9}$$

Likewise, an alternative state function $N_w(\mu, p)$ has the total differential

$$dN_w = \left(\frac{\partial N_w}{\partial \mu}\right)_p d\mu + \left(\frac{\partial N_w}{\partial p}\right)_\mu dp \tag{10}$$

By eliminating dp from both equations, we obtain the total differential for $N_w(\mu, V)$, which implies the relation

$$\left(\frac{\partial N_w}{\partial V}\right)_\mu \left[\left(\frac{\partial V}{\partial N_w}\right)_p + \left(\frac{\partial V}{\partial p}\right)_{N_w}\left(\frac{\partial p}{\partial N_w}\right)_\mu\right] = 1 \tag{11}$$

Applying the chain derivative rule to the last factor,

$$\left(\frac{\partial p}{\partial N_w}\right)_\mu = \left(\frac{\partial p}{\partial V}\right)_\mu \left(\frac{\partial V}{\partial N_w}\right)_\mu \tag{12}$$

and using the definitions in eqs 7 and 8, we obtain a relation between both partial volumes

$$v_\mu \left[1 - \left(\frac{\partial V}{\partial p}\right)_{N_w}\left(\frac{\partial p}{\partial V}\right)_\mu\right] = v_p \tag{13}$$

In the next step, we introduce the compressibility χ of the system as $\chi = -(\partial V/\partial p)_{N_w}/V$. Expressing the volume as $V = AL_z$, where A is the constant surface area and L_z is the repeat distance of the layers, we arrive at the relation

$$v_\mu = \frac{v_p}{1 + \chi L_z\left(\frac{\partial p}{\partial L_z}\right)_\mu} \tag{14}$$

Here, $(\partial p/\partial L_z)_\mu$ is the derivative of the interaction pressure with respect to the repeat distance, that is, the surface separation D plus the thickness of the interacting layers. As seen from eq 14, the difference between both partial volumes arises from the finite compressibility of the system. Because v_p is almost constant as a function of D in the case shown in Figure 5, we conclude that the increase in v_μ at small D is almost entirely due to the influence of the system compressibility and the pressure increase at small D (as seen in Figure 3c).

3.3. Influence of the Surface–Surface Hydrogen-Bonding Capability. An important factor that influences the hydration and adhesion properties of surfaces is the capability of polar surface headgroups to form HBs between themselves. It seems reasonable that surface polarity and in-plane HB capability are correlated. However, there are exceptions of great biological relevance where there is no such correlation, as, for instance, for the most abundant class of phospholipids, the phosphatidylcholine (PC) lipids. Their headgroups are highly polar but incapable of forming HBs as a result of the lack of HB donors.

In this section, we examine the influence of the surface–surface HB capability by modifying the repulsive LJ coefficient C_{12} between the oxygen atoms in OH headgroups. In other words, we tune the effective size σ of the headgroup and by that the closest distance up to which two headgroups can approach. Note that we keep the water–headgroup interactions unchanged. The C_{12} coefficients are listed in Table 1. For surface types V and VI, we use a rather small C_{12} coefficient as provided in the GROMOS force field.[67] With the attractive LJ coefficient being $C_6 = 0.0022$ nm^6 kJ/mol, this corresponds to an effective headgroup diameter of $\sigma = (C_{12}/C_6)^{1/6} = 0.30$ nm. Because the headgroups are arranged on a hexagonal lattice in one plane, the intra- and intersurface hydrogen-bonding capability for these surfaces is considerable, as we show further below. The other extreme of almost completely suppressed HB capability is provided by surface types I, II, and IV. The effective headgroup diameter for these surfaces is $\sigma = 0.40$ nm, and surface type III lies in between.

In the following section, we focus on a detailed comparison of soft surfaces of type IV (with low HB capability) and type V (with high HB capability), which differ only by the repulsive headgroup–headgroup LJ potential. The effect of modifying the effective hydroxyl size can be directly demonstrated by the radial distribution function (RDF) between the oxygen atoms of the same surface. Figure 6a shows the lateral RDF for completely

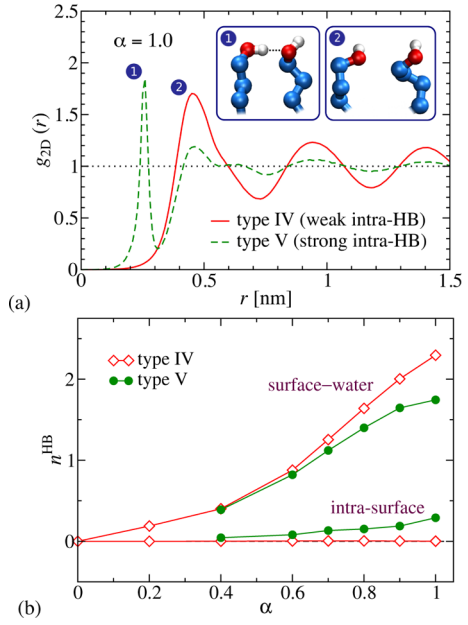

Figure 6. (a) Lateral radial distribution function of headgroup oxygen atoms on completely polar surfaces of types IV and V in contact with water. The other surface in the simulations is placed at a large distance, $D > 2$ nm, in order not to influence the distribution. The insets show snapshots of neighboring surface molecules (1) when they form a HB and (2) when they do not. (b) Number of surface–water and intrasurface HBs per headgroup for a single surface as a function of surface polarity α.

polar ($\alpha = 1$) surface types in the presence of a thick water slab, $D > 2$ nm. For type V, an additional sharp peak appears at a closer distance, indicating that neighboring headgroups form hydrogen bonds, which does not occur in type IV.

The HBs can be directly counted in the simulations by using the standard distance–angle criterion.[79] We distinguish between HBs formed among headgroups and water molecules and HBs

DOI: 10.1021/acs.langmuir.6b01727
Langmuir 2016, 32, 8767–8782

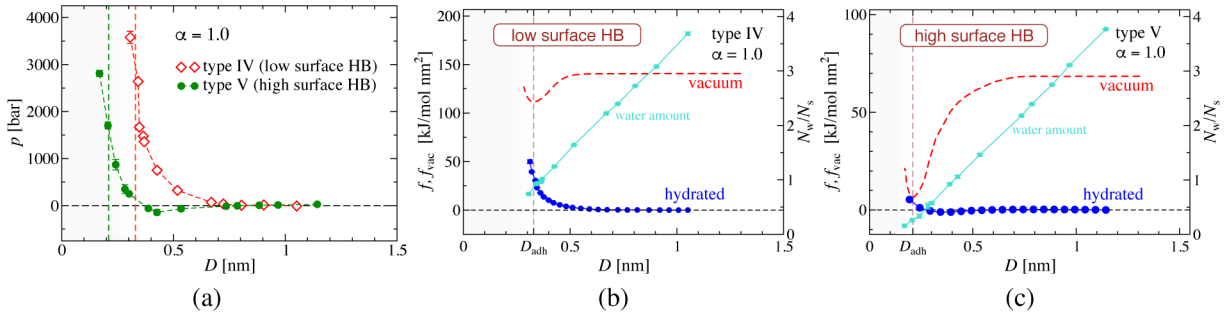

Figure 7. Influence of the surface−surface hydrogen bonding capability on the hydration interaction. (a) Pressure−distance plots for completely polar ($\alpha = 1$) soft surfaces of types IV and V. The dashed vertical lines represent the close-contact separations D_{adh} at which the vacuum free energy is minimal. (b, c) Corresponding free energies of the hydrated and cavitated states. The amount of water in the hydrated and cavitated states is shown by turquoise curves (scale on the right).

formed among the headgroups themselves. In Figure 6b, we compare the number of HBs per headgroup as a function of polarity α for two surface types at large separation. In the case of surface type IV, the surface−surface HBs are almost completely suppressed and their number is negligible. In contrast, the headgroups in surface type V form on average 0.3 intrasurface HB per headgroup for the highest polarity. With increasing polarity α, the headgroups progressively form more HBs with water, in particular, for type IV. Because the type IV headgroups cannot form HBs between themselves, they tend to form more HBs with water molecules than does surface type V. The headgroups of type V, on the other hand, redistribute their HB formation among water and other headgroups.

The hydration pressures for the two surface types, plotted in Figure 7a, show qualitatively similar behavior. Both decay monotonically with separation because of their softness, but they exhibit very different pressure amplitudes. At the same separation D, the high-HB-capability type V surfaces repel much less than the low-HB-capability surfaces of type IV. Also, the close-contact separation D_{adh} (vertical dashed lines in Figure 7a) is 0.12 nm smaller for type V surfaces. Figure 7b,c shows the free energy and the amount of water for both surface types. As can be seen, the type IV surface remains strongly hydrated down to small separations. Expelling all water molecules from the interlamellar region requires enormous pressure; in fact, at the close-contact distance D_{adh} in Figure 7b we still find 0.7 water molecule per headgroup in the hydrated state.

In general, the capability of surface−surface hydrogen-bond formation has at least two major consequences. First, because an increased capability lowers the number of surface−water HBs, it lowers the overall surface hydrophilicity for the same polarity. This is quantified by the reduction of the wetting coefficient k_w for the same α in the interaction diagram (Figure 4b) when we go from surfaces with high headgroup repulsion (types I, II, and IV) to surfaces with low headgroup repulsion (types V and VI). On the other hand, increased hydrogen-bond formation between two opposing surfaces leads to a stronger adhesion in vacuum, f_{vac}^{adh}, which shifts the simulation data to the right in Figure 4b when going from surfaces with low HB capability to surfaces with high HB capability. Systems IV and V with high HB capabilities are therefore shifted to the lower right relative to the other surface types of the same polarity.

Completely polar surfaces with $\alpha = 1$ and high surface−surface HB capability (i.e., types V and VI) have an interesting feature; namely, they attain adhesive properties similar to that of a slab of water. Splitting a slab of water into two half spaces and thereby creating two water−vapor interfaces requires work per surface area corresponding to $f_{vac}^{adh} = 2\gamma$. At the same time, a slab of water in contact with vapor has a wetting coefficient of exactly unity, $k_w = 1$, as follows from eq 1. As seen from the interaction diagram in Figure 4b, both quantities for totally polar surface types V and VI approach $k_w \simeq 1$ and $f_{vac}^{adh}/2\gamma \simeq 1$, in agreement with what would be expected for the interaction between two waterlike surfaces.

However, the wetting coefficients k_w are in both cases slightly larger than the vacuum adhesion energies $f_{vac}^{adh}/2\gamma$. This means that these surfaces are marginally located in the hydration repulsion regime and therefore slightly repel, as also demonstrated by evaluating the hydration free energy for type V in Figure 7c. Completely polar surfaces with large surface−surface HB capabilities are therefore only slightly repulsive.

Interestingly, the completely nonpolar surfaces ($\alpha = 0$), regardless of their type, have almost the same wetting coefficient of $k_w \simeq -0.7$, which corresponds to a contact angle of around $\theta = 134°$, as seen in Figure 4b. In this case, water molecules interact with the surfaces only via dispersion interaction, modeled as LJ potentials in our case, and the exact structural details and surface elastic properties are demonstrated not to play a significant role. The structural details for water−surface interactions start to matter only when the headgroups possess nonvanishing dipole moments.

In our modeling approach, tuning the HB capability via modifying the repulsive C_{12} coefficient also affects the close-contact distance D_{adh} to which the surfaces approach in vacuum. Larger values of C_{12} correspond to larger effective headgroup sizes σ, larger D_{adh}, and consequently smaller f_{vac}^{adh}. Surface types V and VI with small headgroup repulsion therefore have larger f_{vac}^{adh} values than the other surface types.

With our model surfaces, we cover the extreme scenarios of hydrogen-bonding capability. Reality is expected to lie somewhere in between, depending on the surface chemistry, topography, and so forth. Even though the precise surface interactions depend on the molecular details, the overall qualitative adhesion behavior can already be assessed by macroscopic quantities k_w and f_{vac}^{adh}, as demonstrated in Figure 4b.

With the preceding analysis, we assess the qualitative impact of all three control parameters of the model surfaces on the adhesion properties. From the interaction diagram in Figure 4b, we conclude that by far the most important parameter is the polarity α of the surfaces because it primarily determines their hydrophilicity. The second-most-important property regarding the adhesion properties is the surface−surface hydrogen-bonding capability, whereas the elastic properties manifest

DOI: 10.1021/acs.langmuir.6b01727
Langmuir 2016, 32, 8767−8782

mainly in the pressure−distance curves (Figure 3) but do not strongly affect the adhesion properties.

We will now investigate the universality of the adhesion contact angle θ_{adh}, which is defined as the contact angle at which the transition from repulsion to adhesion for particular surface types occurs. According to eq 6, the adhesion transition, defined as $f^{adh} = 0$, occurs when the surface affinity to water is exactly equal to the surface affinity to a second surface. The curves of different surface types in Figure 4b intersect the adhesion diagonal at various locations defined by $k_w^{adh} \equiv k_w(\alpha_{adh}) = f_{vac}^{adh}(\alpha_{adh})/2\gamma$, as listed in Table 2. One extreme case is represented by two surfaces of type I, with fully suppressed HB capability and restrained headgroups, where the adhesive wetting coefficient $k_w^{adh} = 0.11$ is extremely low. The other extreme case, represented by type V with freely mobile and very flexible chains capable of excessive surface−surface HB formation, has a very high value of $k_w^{adh} = 0.76$. This large span of the adhesion values k_w^{adh} at first sight does not seem to point towards universality. But when expressing these values in terms of contact angles $\theta_{adh} = \arccos k_w^{adh}$, the range transforms into a relatively narrow window from 40 to 83°, as shown in Table 2. Most naturally occurring experimentally relevant surfaces probably lie somewhere in between these two extreme scenarios, so a comparatively narrow range around a quasi-universal adhesive contact angle is suggested by our results. In fact, all experimentally reported adhesive contact angles fall into the rather narrow range of $\theta_{adh} \approx 60-80°$,[43−46] consistent with this prediction.

Table 2. Adhesive Properties of Different Surface Types in Terms of the Adhesive Wetting Coefficient k_w^{adh}, the Adhesive Contact Angle (Obtained via $k_w^{adh} = \cos\theta_{adh}$), and the Surface−Surface Adhesive Separation in Vacuum D_{adh} at the Adhesion Transition[a]

	k_w^{adh}	θ_{adh} (deg)	D_{adh} (nm)
type I	0.11	82	0.38
type II	0.26	75	0.36
type III	0.39	67	0.34
type IV	0.24	76	0.32
type V	0.76	40	0.21
type VI	0.62	52	0.29

[a]The adhesive contact angle θ_{adh} is defined as the contact angle at which the system passes from hydration repulsion to dry adhesion.

4. ASYMMETRIC INTERACTION SCENARIOS

So far, we have considered only symmetric scenarios where the interacting surfaces are identical in chemical surface structure and thus have the same contact angles. However, many real situations involve dissimilar surfaces, for example, weak protein−protein interactions,[80] nanoparticles interacting with cell membranes,[81] or membranes interacting with biominerals.[5] Several experimental studies addressed the interactions between dissimilar surfaces and the particularly interesting case of hydrophobic−hydrophilic interfaces.[12−14,41,48−50] The results are very diverse and do not seem to fit into a universal picture. In this section, we address the asymmetric case, where the interacting surfaces have dissimilar polarities α_1 and α_2.

For soft surfaces with a low surface−surface HB capability of type IV, it was recently shown that the asymmetric scenario can be described by simple combination rules based on the sum of the contact angles.[66] Here we extend the analysis to high-HB-capability surfaces of type V.

The situation of dissimilar surfaces leads to qualitatively similar behavior as the symmetric situation. Depending on the surface polarities, the interaction behavior can be cast into one of three regimes: cavitation, dry adhesion, or hydration repulsion. The free energy of the adhesive state given by eq 6 for the symmetric case can be straightforwardly generalized to the asymmetric case and reads

$$f^{adh} = \gamma(k_{w1} + k_{w2}) - f_{vac}^{adh} \tag{15}$$

The first term is the cavitation free energy of water between surfaces 1 and 2 at large separations, that is, $f_{vac}(D \to \infty) = (\gamma_{s1,v} - \gamma_{s1,w}) + (\gamma_{s2,v} - \gamma_{s2,w}) = \gamma(k_{w1} + k_{w2})$, which is simply the sum of the independent contributions from both surfaces. The second term accounts for the surface−surface adhesion free energy in vacuum, now evaluated for the case of dissimilar surfaces. This term has to be determined independently via simulations for each pair of surfaces. However, later on we will establish an approximate combination rule that allows for a simple estimate of this term. For similar surfaces, eq 15

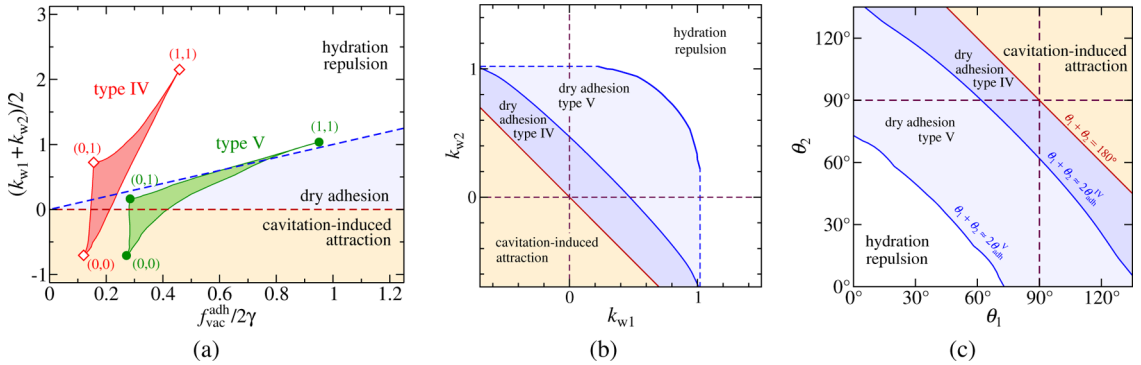

Figure 8. (a) Interaction diagram in terms of the average wetting coefficient of both surfaces $(k_{w1} + k_{w2})/2$ versus the rescaled adhesive free energy f_{vac}^{adh} between the two surfaces in vacuum. The dashed triangular zones show the range for all polarity combinations α_1 and α_2 for surfaces of type IV and V extracted from simulations. The data points at the vertices denote the three limiting cases in terms of the polarities (α_1, α_2). (b) Interaction diagram for two interacting surfaces of the same type in terms of their respective wetting coefficients k_{w1} and k_{w2}. The orange shaded region represents the regime of cavitation-induced attraction, which is universally given by eqs 16 and 17 and thus the same for all surface types. The blue regions of darker and lighter shades represent the dry adhesion regime for type IV and type V surfaces, respectively. The white region is the hydration repulsion regime. (c) The same diagram as in (b) expressed in terms of contact angles θ_1 and θ_2.

DOI: 10.1021/acs.langmuir.6b01727
Langmuir 2016, 32, 8767−8782

simplifies to our previous result in eq 6. Note that the sum of the surface wetting coefficients, as in eq 15, has previously been used to interpret experimental force measurements.[49]

For asymmetric combinations of surface polarities, we present the interaction diagram in Figure 8a, which is similar to the interaction diagram for symmetric surfaces in Figure 4b. On the ordinate, the wetting coefficient is replaced by the mean of the wetting coefficients of both surfaces $(k_{w1} + k_{w2})/2$, and the vacuum adhesion free energy on the abscissa, $f_{vac}^{adh}/2\gamma$, now depends on the general dissimilar polarities of the surfaces. On the basis of the experimental simulation results, all possible combinations of surface polarities α_1 and α_2 ranging from 0 to 1 are denoted by shaded zones for surface types IV and V. The zones have the shape of distorted triangles, where the three vertices correspond to the limiting polarities: both surfaces are completely polar ($\alpha_1 = 1$, $\alpha_2 = 1$), both surfaces are completely nonpolar ($\alpha_1 = 0$, $\alpha_2 = 0$), and surface combinations of completely asymmetric polar−nonpolar ($\alpha_1 = 0$, $\alpha_2 = 1$). The bottom-right edge of the triangular zones corresponds to the symmetric situation with $\alpha_1 = \alpha_2$, which are exactly the curves shown previously in Figure 4b. Going from the completely nonpolar scenario ($\alpha_1 = \alpha_2 = 0$) by polarizing one of the surfaces to $\alpha_2 = 1$, we follow an almost vertical line. The almost vertical trend is due to the fact that the surface−surface interaction f_{vac}^{adh} is not influenced by the polarity of one surface if the other one is nonpolar. However, small deviations from a vertical line occur, probably resulting from weak hydration-induced rearrangements of the headgroups of the polar surface. The upper edge of the triangular zones corresponds to the situation where one surface is completely polar, $\alpha_2 = 1$, and the other surface is changing from $\alpha_1 = 0$ to $\alpha_1 = 1$.

An insightful interaction diagram is obtained by plotting the individual wetting coefficients or the contact angles of the surfaces on separate axes, as shown in Figure 8b,c for surface types IV and V. The three interaction regimes are indicated by the same shaded colors as in Figure 8a. In the corner where both surfaces are polar, we find hydration repulsion, whereas in the opposite corner where both surfaces are nonpolar, we find cavitation-induced attraction. In between these limiting regimes, there is an intermediate regime of dry adhesion. These three regimes extend into the mixed corners, where one surface is polar and the other one nonpolar. In other words, we find hydration repulsion for every nonpolar surface if the other surface is polar enough, and conversely, we find cavitation-induced attraction for a rather polar surface if the other surface is hydrophobic enough.

We will now present simple scaling expressions for the transitions among the hydration repulsion, the dry adhesion, and the cavitation-induced attraction regimes that are shown in Figure 8b,c. The cavitation free energy for a water slab between two dissimilar surfaces at large separation is given by the first term in eq 15, which implies a cavitation transition at

$$k_{w1} + k_{w2} = 0 \tag{16}$$

By expressing this relation in terms of contact angles and using the sum-to-product rule $\cos\theta_1 + \cos\theta_2 = 2\cos[(\theta_1 + \theta_2)/2]\cos[(\theta_1 - \theta_2)/2]$, we arrive at[66]

$$\theta_1 + \theta_2 = 180° \tag{17}$$

For the symmetric case, we recover the known transition threshold $\theta_1 = \theta_2 = 90°$. The cavitation transition given by eqs 16 and 17, shown by straight red lines in Figure 8b,c, is universal and for given contact angles independent of all other surface properties.

Adjacent to the cavitation regime, the blue-shaded areas correspond to the dry adhesion regime. This region is for type V (lighter shade) considerably broader than for type IV (darker shade) due to the much larger value of the sum of the wetting coefficients $k_{w1} + k_{w2}$ at the adhesion transition for surface type V, as can be seen in Figure 8a. The adhesion transitions in Figure 8c can be empirically approximated as

$$\theta_1 + \theta_2 \approx 2\theta_{adh} \tag{18}$$

This result was recently demonstrated for type IV surfaces,[66] but as seen in Figure 8c, it works as well for type V. In the next section, we derive the adhesion law in eq 18 for surface interaction by using perturbative combination rules.

4.1. Combination Rules. An interesting and in practice very important question is whether it is possible to infer the interactions between dissimilar surfaces, knowing the interactions of the respective symmetric cases. Using perturbation analysis, we show that this is indeed possible within good accuracy.

The cavitation free energy is trivially generalized as $2\gamma k_w \rightarrow \gamma(k_{w1} + k_{w2})$, as already established in eq 15. The vacuum adhesion energy, f_{vac}^{adh}, on the other hand, cannot be easily generalized to asymmetric surfaces. Nevertheless, we can decompose it into the contribution w_{LJ} originating from LJ interactions and the polar contribution w_α stemming from dipole−dipole interactions between the surfaces, leading to the sum

$$f_{vac}^{adh}(\alpha_1, \alpha_2) = w_{LJ} + w_\alpha(\alpha_1, \alpha_2) \tag{19}$$

By this decomposition, the second term is zero for completely nonpolar surfaces ($\alpha_1 = \alpha_2 = 0$). To good approximation, we can assume the LJ contribution to be independent of surface polarity. Minor deviations can occur because the dipoles will in general affect the adhesive close-contact distance D_{adh}, which in turn influences the surface−surface LJ interaction.

The dipole contribution w_α arises from interactions between dipoles on opposing surfaces and is hence proportional to the product of the dipole moments on the two surfaces. Therefore, we expect a geometric combination rule for the polar contribution for an asymmetric pair of surfaces,

$$w_\alpha(\alpha_1, \alpha_2) = \sqrt{w_\alpha(\alpha_1)\, w_\alpha(\alpha_2)} \tag{20}$$

where $w_\alpha(\alpha) \equiv w_\alpha(\alpha, \alpha)$ is the dipole interaction for the symmetric case. A similar combination rule was established earlier on the basis of experimental data.[48] The polar contribution $w_\alpha(\alpha_1, \alpha_2)$ can be obtained from simulations by measuring the adhesion free energy in vacuum, f_{vac}^{adh}, and subtracting the LJ part $w_{LJ} = f_{vac}^{adh}(\alpha_1 = 0, \alpha_2 = 0)$, which corresponds to the adhesion free energy in vacuum for completely nonpolar surfaces. In Figure 9, we verify the combination rule (eq 20) for surface types IV and V by a correlation plot of the directly measured polar contribution $w_\alpha(\alpha_1, \alpha_2)$ from simulations versus the computed value according to eq 20. The agreement is very good, especially for surface type IV. Some smaller discrepancies appear for cases in which one of the surfaces is very hydrophobic, that is, for small values of $w_\alpha(\alpha_1, \alpha_2)$. But in those cases, the w_α contribution is small compared to the overall f_{vac}^{adh} and is rather negligible. We conclude that the combination rule in eq 20 is an accurate

DOI: 10.1021/acs.langmuir.6b01727
Langmuir 2016, 32, 8767−8782

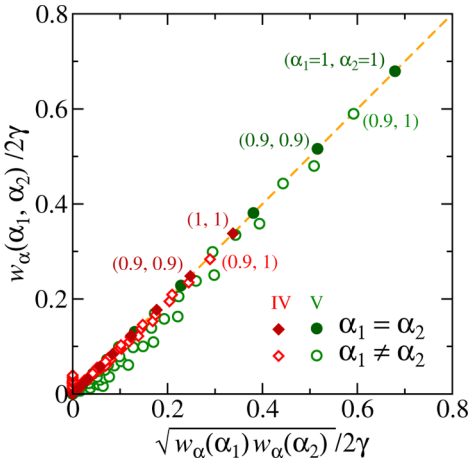

Figure 9. Correlation plot of the simulated and the estimated polar part of the vacuum adhesion free energies via eq 20 for various combinations of α_1 and α_2 for surface types IV and V.

approximation of the polar interaction between asymmetric surfaces.

We now return to the reasoning behind the approximate adhesion law given by eq 18. As we already noted, it is only approximate and depends on the exact functional behavior of $f_{\mathrm{vac}}^{\mathrm{adh}}$ as a function of k_{w1} and k_{w2}. By merging eqs 15, 19, and 20 and considering polar contribution w_α to be a function of the wetting coefficient, the adhesion transition $f^{\mathrm{adh}} = 0$ can be expressed as

$$\gamma(k_{\mathrm{w1}} + k_{\mathrm{w2}}) = w_{\mathrm{LJ}} + \sqrt{w_\alpha(k_{\mathrm{w1}})\, w_\alpha(k_{\mathrm{w2}})} \tag{21}$$

The combinations of k_{w1} and k_{w2} for which the adhesion transition occurs depend on the exact functional form of $w_\alpha(k_{\mathrm{w}})$, which is surface-specific but in general is monotonically increasing, as can be seen for all surface types considered by us in Figure 4b. To proceed with our derivation, we consider the simplest nontrivial form, namely, a polar contribution w_α that linearly increases with k_{w},

$$w_\alpha(k_{\mathrm{w}}) = w_\alpha^0 + 2c\gamma k_{\mathrm{w}} \tag{22}$$

where w_α^0 and c are free parameters. As can be seen in Figure 4b, this assumptions is a good approximation for surfaces with low surface HB capability (types I, II, and IV), whereas for the surfaces with high HB capability (types V and VI) it is only a rough estimate. Inserting eq 22 into eq 21 and expanding it to linear order in k_{w1} and k_{w2} yields the general relation for the adhesion transition

$$k_{\mathrm{w1}} + k_{\mathrm{w2}} = 2\cos\theta_{\mathrm{adh}} \tag{23}$$

where we have defined the adhesive contact angle as

$$\cos\theta_{\mathrm{adh}} = \frac{w_{\mathrm{LJ}} + w_\alpha^0}{\gamma(1 - c)} \tag{24}$$

As a further approximation, we can expand the cosine in eq 23 in a Taylor series around $\theta = \pi/2$ as $\cos\theta \simeq \pi/2 - \theta$, which gives the expression for the adhesion transition as $\theta_1 + \theta_2 \approx 2\theta_{\mathrm{adh}}$, as already presented in eq 18. As should have become clear from the derivation, which involves a number of simplifications, the dry adhesion law in eq 18 is an approximation and becomes accurate for nearly symmetric scenarios where both contact angles are quite similar. On the other hand, for considerably asymmetric scenarios, where one surface is very polar and the other one is completely nonpolar, minor deviations from the simple linear relationship given by eq 18 are in fact observed (Figure 8c).

5. FINITE-SIZE EFFECTS AND HETEROGENEOUS SYSTEMS

5.1. Finite-Size Effects. So far, we have considered only laterally extended surfaces and have disregarded finite-size or edge effects. In reality, edge effects play an important role for small-enough interacting surfaces, for example, for small colloidal particles.

Strictly speaking, the cavitation law, $\theta_1 + \theta_2 = 180°$, in eq 17 is valid only for large-enough surfaces and small separations, where the atmospheric pressure is negligible. However, the atmospheric pressure and the water−vapor interface that forms at the lateral edges of the finite surfaces oppose cavitation. As a result, cavitation appears only below a critical surface separation D_{c}.

We now estimate finite-size effects on the cavitation transition, as was done previously for the symmetric case.[34,36,82] A system with lateral dimensions $L \times L$ (Figure 10a) has in the hydrated state a free energy

$$F = L^2\gamma_{\mathrm{s1w}} + L^2\gamma_{\mathrm{s2w}} \tag{25}$$

whereas in the cavitated state the free energy is

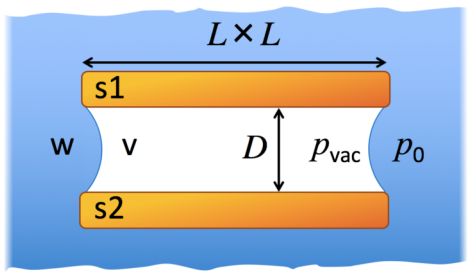

(a)

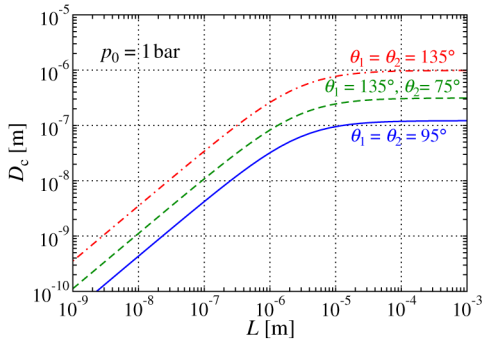

(b)

Figure 10. (a) Schematic illustration of water cavitation between finite-sized parallel surfaces s1 and s2. Water (w) is depleted from the interlamellar region and leaves a vapor phase (v) behind. (b) Critical distance D_{c} below which cavitation occurs (eq 27) as a function of lateral surface size L for different combinations of the two contact angles θ_1 and θ_2 at atmospheric pressure p_0 = 1 bar.

DOI: 10.1021/acs.langmuir.6b01727
Langmuir 2016, 32, 8767−8782

$$F_{vac} = L^2\gamma_{s1v} + L^2\gamma_{s2v} + 4LD\gamma + (p_0 - p_{vap})L^2D \quad (26)$$

Here, the third term, proportional to LD, is the contribution from the water−vapor interface formed between both surfaces along the circumference. For simplicity, we assume a square shape of the two opposing surfaces such that the total length of the circumference is $4L$ (Figure 10a). The last term in eq 26 represents the work against the external pressure due to removing the water from the region between the surfaces. Typically, the atmospheric pressure is $p_0 = 1$ bar and thus much larger than the saturated vapor pressure, p_{vap}, which can be neglected. The water−vapor interface at the perimeter is curved as a result of the difference in the pressure $p_0 - p_{vap}$, with the corresponding radius of $R = \gamma/(p_0 - p_{vac}) \approx 0.7 \times 10^{-6}$ m. This curvature can be neglected when considering the water−vapor surface contribution for small surface separations in the nanometer range. Cavitation occurs for $F_{vac} < F$, which yields the critical distance for the general asymmetric case

$$D_c = -\frac{\gamma(\cos\theta_1 + \cos\theta_2)}{p_0 + (4\gamma/L)} \quad (27)$$

We see that edge effects play a significant role for lateral system sizes of $L \lesssim 4\gamma/p_0 \approx 10^{-6}$m.

Figure 10b shows the critical surface cavitation separation D_c, based on eq 27, as a function of the lateral size L for three different contact angle combinations. For large surface sizes $L \gtrsim 10^{-6}$ m, the critical cavitation separation saturates at values much larger than the nanometer scale discussed in this work. For smaller lateral sizes $L \lesssim 10^{-6}$ m, the critical separation becomes comparable to the lateral system size, $D_c \simeq -(L/4)(\cos\theta_1 + \cos\theta_2)$.

Another important aspect that arises for smaller surface areas is that the relative fluctuations in the number of water molecules between surfaces become large. Because cavitation is hindered by significant free energy barriers,[15,16,34,35,83] fluctuations play a crucial role in barrier crossing events.[26,27,29,30,38,84] Namely, surfaces in the hydrated state experience fluctuations in the intersurface number of water molecules δN_w and consequently in the interaction pressure $\delta p \propto \delta N_w$. Because the relative water-number fluctuations scale as $\delta N_w/N_w \propto N_w^{-1/2}$, fluctuations in the hydration pressure scale inversely with the lateral size of the surface $\delta p \propto L^{-1}$. A detailed analysis suggests that hydration fluctuations indeed become significant for surface sizes below several tens of nanometers.[85]

5.2. Heterogeneous Systems. Until now, we have considered flat surfaces with only one chemical type of headgroup. However, biological as well as technologically relevant surfaces are typically characterized by heterogeneous compositions of different headgroup types. A prototypical example are surfaces with a mixture of polar OH and nonpolar CH_3 headgroups. The fraction of OH groups on the surface can be described by the parameter ξ, where $\xi = 1$ corresponds to a fully OH-terminated polar surface and $\xi = 0$ corresponds to a fully CH_3-terminated nonpolar surface. Heterogeneous surfaces with arbitrary distributions of polar and nonpolar headgroups are beyond the scope of this work. The wetting behavior of water between two plates with heterogeneous headgroup distributions has been thoroughly analyzed in earlier studies.[60,86]

Here, we only briefly discuss two limiting scenarios of headgroup distributions, which have also been considered in the context of electrostatic interactions.[87]

In one extreme case, the polar and nonpolar groups on the surfaces are completely randomly distributed down to the molecular scale (Figure 11a). In this case, the surfaces roughly act as if they were effectively homogeneous, with an effective polarity α that depends on the OH fraction ξ.

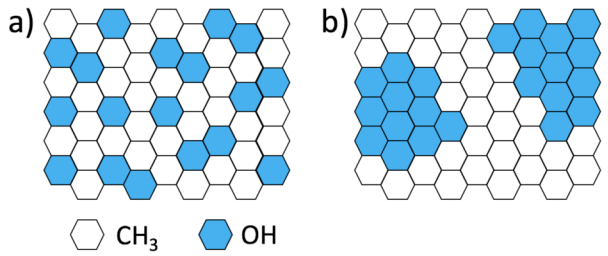

Figure 11. Illustration of the two limiting scenarios of heterogeneous surfaces consisting of polar and nonpolar groups. (a) Completely random distribution, with the surface acting as effectively homogeneous, and (b) segregation into polar and nonpolar patches of mesoscopic size.

In the other limiting scenario, the polar and nonpolar groups are locally segregated and form mesoscale patches on the surfaces (Figure 11b). In this case, we assume that edge effects of the patches contribute negligibly to the total interaction and therefore add up to the free energy contributions stemming from the overlapping patches. If we neglect correlations between interacting surface patches, then the free energy in the close-contact state follows as

$$f_\xi^{adh} \simeq \xi^2 f_{11}^{adh} + 2\xi(1-\xi)f_{01}^{adh} + (1-\xi)^2 f_{00}^{adh} \quad (28)$$

Here, f_{11}^{adh}, f_{01}^{adh}, and f_{00}^{adh} correspond to the adhesion free energies of the polar−polar, polar−nonpolar, and nonpolar−nonpolar surfaces, respectively. The prefactors denote the fractions of the corresponding overlapping pairs.

The above analysis is suitable for quenched distributions, that is, distributions of headgroups that do not laterally reorganize with time. This approximation is valid for covalently grafted surface molecules. The scenario more relevant for self-assembled surfaces, such as lipid membranes, is the annealed scenario, where the surface molecules can diffuse in lateral directions and reorganize themselves in order to minimize the free energy.

6. CONCLUSIONS

Water-mediated interactions are ubiquitous in biology and technological processes. Their characteristics depend on the surfaces' chemical details, which can become very complex, for instance, for the case of biomembranes. However, important lessons about the interaction mechanisms can be learned from studies with simplified models of interacting surfaces. In recent years, atomistic computer simulations that account for the chemical potential of water and atomistic surface details have made substantial progress in the description of interfacial forces across aqueous layers.[52,55,64] In the present work, we employed molecular dynamics simulations to investigate interactions between hydroxylated model surfaces with tunable polarities, mechanical stiffness, and hydrogen-bonding capability. On the basis of free energy considerations, we have identified three interaction regimes: hydration repulsion for very polar surfaces, dry adhesion for intermediate polarities, and cavitation-induced long-range attraction for low surface polarities. The transitions

DOI: 10.1021/acs.langmuir.6b01727
Langmuir 2016, 32, 8767−8782

among these regimes can be universally expressed in terms of the affinities of the involved surfaces for water binding as well as their mutual binding strength. These two affinities tend to be correlated because they typically have similar dependences on surface parameters such as the dipolar strength of functional surface groups. The transitions among the three interaction regimes are to good approximation related to the sum of the two surface contact angles. Whereas the cavitation transition occurs universally when the sum of both contact angles is above 180° (eq 17), dry adhesion is obtained when the sum of the surface contact angles exceeds approximately twice the critical adhesive contact angle $2\theta_{adh}$. The adhesive contact angle is highly surface-specific, but for the surface types considered by us, it lies in the typical range of $\theta_{adh} \approx 40-80°$. Our analysis shows that the adhesive contact angle θ_{adh} depends on several surface properties. For stiff, crystalline surfaces without hydrogen-bonding capability, the value of θ_{adh} exceeds 80°. Extremely soft surfaces with very mobile groups capable of forming intra- and intersurface hydrogen bonds, on the other hand, can exhibit values of θ_{adh} as low as 40°.

An important conclusion from our work is that it appears possible to design surface combinations with extremely low or even vanishing adhesive contact angles θ_{adh}. Such surfaces would bind to each other very tightly in a dry-adhesion complex, despite their pronounced hydrophilicity.

One major open question in the field of hydration interactions is how surface charges and ions influence the adhesion properties. The adsorption of ions to various interfaces, including the water−vapor interface, depends on the ion hydration properties.[88−90] The adsorbed ions reorganize the solvent in their vicinity and by that influence the hydration force among various hydrophilic surfaces, which can be either enhanced or even entirely suppressed.[91−93] The relation between electrostatic interactions and the hydration force is an open field that will be tackled in future studies.

■ ASSOCIATED CONTENT

Supporting Information

The Supporting Information is available free of charge on the ACS Publications website at DOI: 10.1021/acs.langmuir.6b01727.

Simulation details, evaluating wetting coefficients, interaction pressure at a prescribed chemical potential, and the relation between density profiles and pressure−distance curves (PDF)

■ AUTHOR INFORMATION

Corresponding Authors

*E-mail: matej.kanduc@helmholtz-berlin.de.
*E-mail: rnetz@physik.fu-berlin.de

Notes

The authors declare no competing financial interest.

Biographies

Matej Kanduč studied physics at the University of Ljubljana, Slovenia, where he received his Ph.D. in physics in 2010. As a fellow of the Alexander von Humboldt Foundation, he joined the bio- and soft-matter physics group of Roland R. Netz at the Technical University of Munich and the Free University of Berlin. Since 2015, he has worked at the Institute of Soft Matter and Functional Materials at Helmholtz-Zentrum Berlin. His main research focuses on the computer modeling of biological and soft-matter systems.

Alexander Schlaich studied physics at the University of Stuttgart where he received his diploma degree in 2011. In 2012, he was a fellow of the HPC Europa2 program at Università di Roma La Sapienza. Since 2012, he has been a Ph.D. student in the group of Roland R. Netz at the Free University of Berlin, where his research is focused on the interaction between biological and synthetic functionalized surfaces in aqueous environments.

Emanuel Schneck studied physics at the Technical University of Munich (TUM) and received his Ph.D. in physics in 2010 from

DOI: 10.1021/acs.langmuir.6b01727
Langmuir 2016, 32, 8767−8782

Heidelberg University. After postdoctoral assignments at TUM and the Free University of Berlin, he went to Institut Laue-Langevin (Grenoble, France) as a Marie Curie fellow in 2012. Since 2014, he has been research group leader at the Max Planck Institute of Colloids and Interfaces in Potsdam, supported by an Emmy-Noether grant from the German Research Foundation (DFG). His current research is focused on interfacial forces and on the structural investigation of biological and biotechnologically relevant soft interfaces, mainly using X-ray and neutron scattering techniques.

Roland R. Netz studied physics at the Technical University of Berlin and at MIT and received his Ph.D. in 1994 from the University of Cologne. After postdoctoral assignments at Tel-Aviv University, the University of California—Santa Barbara, Seattle, Institute Charles Sadron in Strasbourg, and CEA in Paris, he was a research associate at the Max Planck Institute for Colloids and Interfaces in Potsdam. He was appointed associate professor of physics at Ludwig-Maximilian University of Munich in 2002 and full professor of physics at the Technical University of Munich in 2004. Since 2011, he has held a chair in theoretical bio- and soft-matter physics at the Free University of Berlin.

■ ACKNOWLEDGMENTS

We acknowledge funding from the Deutsche Forschungsgemeinschaft (DFG) via grant SFB 1112 and via Emmy-Noether grant SCHN 1396/1.

■ REFERENCES

(1) Evans, D. F.; Wennerström, H. *The Colloidal Domain: Where Physics, Chemistry, Biology, and Technology Meet*; Wiley-VCH: New York, 1999.
(2) Mouritsen, O. G. *Life - As a Matter of Fat*; Springer: Heidelberg, 2005.
(3) Eggens, I.; Fenderson, B.; Toyokuni, T.; Dean, B.; Stroud, M.; Hakomori, S. Specific interaction between Lex and Lex determinants. A possible basis for cell recognition in preimplantation embryos and in embryonal carcinoma cells. *J. Biol. Chem.* **1989**, *264*, 9476.
(4) Lau, P. C. Y.; Lindhout, T.; Beveridge, T. J.; Dutcher, J. R.; Lam, J. S. Differential Lipopolysaccharide Core Capping Leads to Quantitative and Correlated Modifications of Mechanical and Structural Properties in Pseudomonas aeruginosa Biofilms. *J. Bacteriol.* **2009**, *191*, 6618−6631.
(5) Faivre, D.; Böttger, L.; Matzanke, B.; Schüler, D. Intracellular Magnetite Biomineralization in Bacteria Proceeds by a Distinct Pathway Involving Membrane-Bound Ferritin and an Iron(II) Species. *Angew. Chem., Int. Ed.* **2007**, *46*, 8495−8499.
(6) Rosenhahn, A.; Schilp, S.; Kreuzer, H. J.; Grunze, M. The role of inert surface chemistry in marine biofouling prevention. *Phys. Chem. Chem. Phys.* **2010**, *12*, 4275−4286.
(7) Lipowsky, R.; Sackmann, E. *Structure and Dynamics of Membranes: I. From Cells to Vesicles/II. Generic and Specific Interactions*; Elsevier, 1995.
(8) Maître, J.-L.; Berthoumieux, H.; Krens, S. F. G.; Salbreux, G.; Jülicher, F.; Paluch, E.; Heisenberg, C.-P. Adhesion Functions in Cell Sorting by Mechanically Coupling the Cortices of Adhering Cells. *Science* **2012**, *338*, 253−256.
(9) Raviv, U.; Giasson, S.; Kampf, N.; Gohy, J.-F.; Jerome, R.; Klein, J. Lubrication by charged polymers. *Nature* **2003**, *425*, 163−165.
(10) Liu, K.; Jiang, L. Bio-Inspired Self-Cleaning Surfaces. *Annu. Rev. Mater. Res.* **2012**, *42*, 231−263.
(11) Israelachvili, J. *Intermolecular and Surface Forces*; Academic: London, 1992.
(12) Christenson, H. K.; Claesson, P. M. Direct measurements of the force between hydrophobic surfaces in water. *Adv. Colloid Interface Sci.* **2001**, *91*, 391−436.
(13) Freitas, A. M.; Sharma, M. M. Detachment of Particles from Surfaces: An AFM Study. *J. Colloid Interface Sci.* **2001**, *233*, 73−82.
(14) Faghihnejad, A.; Zeng, H. Interaction Mechanism between Hydrophobic and Hydrophilic Surfaces: Using Polystyrene and Mica as a Model System. *Langmuir* **2013**, *29*, 12443−12451.
(15) Bratko, D.; Curtis, R. A.; Blanch, H. W.; Prausnitz, J. M. Interaction between hydrophobic surfaces with metastable intervening liquid. *J. Chem. Phys.* **2001**, *115*, 3873−3877.
(16) Huang, X.; Margulis, C. J.; Berne, B. J. Dewetting-induced collapse of hydrophobic particles. *Proc. Natl. Acad. Sci. U. S. A.* **2003**, *100*, 11953−11958.
(17) Choudhury, N.; Pettitt, B. M. On the Mechanism of Hydrophobic Association of Nanoscopic Solutes. *J. Am. Chem. Soc.* **2005**, *127*, 3556−3567.
(18) Parsegian, V.; Fuller, N.; Rand, R. Measured work of deformation and repulsion of lecithin bilayers. *Proc. Natl. Acad. Sci. U. S. A.* **1979**, *76*, 2750−2754.
(19) Rand, R.; Parsegian, V. Hydration forces between phospholipid bilayers. *Biochim. Biophys. Acta, Rev. Biomembr.* **1989**, *988*, 351−376.
(20) Israelachvili, J. N.; Pashley, R. M. Molecular layering of water at surfaces and origin of repulsive hydration forces. *Nature* **1983**, *306*, 249−250.
(21) Marra, J.; Israelachvili, J. Direct measurements of forces between phosphatidylcholine and phosphatidylethanolamine bilayers in aqueous electrolyte solutions. *Biochemistry* **1985**, *24*, 4608−4618.
(22) Pashley, R. DLVO and hydration forces between mica surfaces in Li^+, Na^+, K^+, and Cs^+ electrolyte solutions: A correlation of double-layer and hydration forces with surface cation exchange properties. *J. Colloid Interface Sci.* **1981**, *83*, 531−546.
(23) Israelachvili, J.; Wennerström, H. Role of hydration and water structure in biological and colloidal interactions. *Nature* **1996**, *379*, 219−225.
(24) Parsegian, V.; Zemb, T. Hydration forces: Observations, explanations, expectations, questions. *Curr. Opin. Colloid Interface Sci.* **2011**, *16*, 618−624.
(25) Chandler, D. Interfaces and the driving force of hydrophobic assembly. *Nature* **2005**, *437*, 640−647.
(26) Godawat, R.; Jamadagni, S. N.; Garde, S. Characterizing hydrophobicity of interfaces by using cavity formation, solute binding, and water correlations. *Proc. Natl. Acad. Sci. U. S. A.* **2009**, *106*, 15119−15124.
(27) Patel, A. J.; Varilly, P.; Chandler, D. Fluctuations of Water near Extended Hydrophobic and Hydrophilic Surfaces. *J. Phys. Chem. B* **2010**, *114*, 1632−1637.
(28) Jamadagni, S. N.; Godawat, R.; Garde, S. Hydrophobicity of Proteins and Interfaces: Insights from Density Fluctuations. Annu. Rev. Chem. *Annu. Rev. Chem. Biomol. Eng.* **2011**, *2*, 147−171.
(29) Patel, A. J.; Varilly, P.; Jamadagni, S. N.; Acharya, H.; Garde, S.; Chandler, D. Extended surfaces modulate hydrophobic interactions of neighboring solutes. *Proc. Natl. Acad. Sci. U. S. A.* **2011**, *108*, 17678−17683.
(30) Patel, A. J.; Varilly, P.; Jamadagni, S. N.; Hagan, M. F.; Chandler, D.; Garde, S. Sitting at the Edge: How Biomolecules use Hydro-

DOI: 10.1021/acs.langmuir.6b01727
Langmuir 2016, 32, 8767−8782

phobicity to Tune Their Interactions and Function. *J. Phys. Chem. B* **2012**, *116*, 2498−2503.
(31) Luzar, A.; Bratko, D.; Blum, L. Monte Carlo simulation of hydrophobic interaction. *J. Chem. Phys.* **1987**, *86*, 2955−2959.
(32) Wallqvist, A.; Berne, B. J. Computer Simulation of Hydrophobic Hydration Forces on Stacked Plates at Short Range. *J. Phys. Chem.* **1995**, *99*, 2893−2899.
(33) Lum, K.; Chandler, D.; Weeks, J. D. Hydrophobicity at Small and Large Length Scales. *J. Phys. Chem. B* **1999**, *103*, 4570−4577.
(34) Lum, K.; Luzar, A. Pathway to surface-induced phase transition of a confined fluid. *Phys. Rev. E: Stat. Phys., Plasmas, Fluids, Relat. Interdiscip. Top.* **1997**, *56*, R6283−R6286.
(35) Leung, K.; Luzar, A.; Bratko, D. Dynamics of Capillary Drying in Water. *Phys. Rev. Lett.* **2003**, *90*, 065502.
(36) Luzar, A. Activation Barrier Scaling for the Spontaneous Evaporation of Confined Water. *J. Phys. Chem. B* **2004**, *108*, 19859−19866.
(37) Sharma, S.; Debenedetti, P. G. Evaporation rate of water in hydrophobic confinement. *Proc. Natl. Acad. Sci. U. S. A.* **2012**, *109*, 4365−4370.
(38) Remsing, R. C.; Xi, E.; Vembanur, S.; Sharma, S.; Debenedetti, P. G.; Garde, S.; Patel, A. J. Pathways to dewetting in hydrophobic confinement. *Proc. Natl. Acad. Sci. U. S. A.* **2015**, *112*, 8181−8186.
(39) Wood, J.; Sharma, R. How Long Is the Long-Range Hydrophobic Attraction? *Langmuir* **1995**, *11*, 4797−4802.
(40) Mastropietro, D. J.; Ducker, W. A. Forces between Hydrophobic Solids in Concentrated Aqueous Salt Solution. *Phys. Rev. Lett.* **2012**, *108*, 106101.
(41) Meyer, E. E.; Rosenberg, K. J.; Israelachvili, J. Recent progress in understanding hydrophobic interactions. *Proc. Natl. Acad. Sci. U. S. A.* **2006**, *103*, 15739−15746.
(42) Donaldson, S. H.; Røyne, A.; Kristiansen, K.; Rapp, M. V.; Das, S.; Gebbie, M. A.; Lee, D. W.; Stock, P.; Valtiner, M.; Israelachvili, J. Developing a General Interaction Potential for Hydrophobic and Hydrophilic Interactions. *Langmuir* **2015**, *31*, 2051−2064.
(43) Berg, J. M.; Eriksson, L. G. T.; Claesson, P. M.; Borve, K. G. N. Three-Component Langmuir-Blodgett Films with a Controllable Degree of Polarity. *Langmuir* **1994**, *10*, 1225−1234.
(44) Vogler, E. A. Structure and reactivity of water at biomaterial surfaces. *Adv. Colloid Interface Sci.* **1998**, *74*, 69−117.
(45) Yoon, R.-H.; Ravishankar, S. Long-Range Hydrophobic Forces between Mica Surfaces in Dodecylammonium Chloride Solutions in the Presence of Dodecanol. *J. Colloid Interface Sci.* **1996**, *179*, 391−402.
(46) Ishida, N.; Kinoshita, N.; Miyahara, M.; Higashitani, K. Effects of Hydrophobizing Methods of Surfaces on the Interaction in Aqueous Solutions. *J. Colloid Interface Sci.* **1999**, *216*, 387−393.
(47) Schwierz, N.; Horinek, D.; Liese, S.; Pirzer, T.; Balzer, B. N.; Hugel, T.; Netz, R. R. On the Relationship between Peptide Adsorption Resistance and Surface Contact Angle: A Combined Experimental and Simulation Single-Molecule Study. *J. Am. Chem. Soc.* **2012**, *134*, 19628−19638.
(48) Yoon, R.-H.; Flinn, D. H.; Rabinovich, Y. I. Hydrophobic Interactions between Dissimilar Surfaces. *J. Colloid Interface Sci.* **1997**, *185*, 363−370.
(49) Lee, J.-H.; Meredith, J. C. Non-DLVO Silica Interaction Forces in NMP-Water Mixtures. II. An Asymmetric System. *Langmuir* **2011**, *27*, 10000−10006.
(50) Troncoso, P.; Saavedra, J. H.; Acuna, S. M. A.; Jeldres, R.; Concha, F.; Toledo, P. G. Nanoscale adhesive forces between silica surfaces in aqueous solutions. *J. Colloid Interface Sci.* **2014**, *424*, 56−61.
(51) Choudhury, N.; Pettitt, B. M. Enthalpy-Entropy Contributions to the Potential of Mean Force of Nanoscopic Hydrophobic Solutes. *J. Phys. Chem. B* **2006**, *110*, 8459−8463.
(52) Pertsin, A.; Platonov, D.; Grunze, M. Origin of Short-Range Repulsion between Hydrated Phospholipid Bilayers: A Computer Simulation Study. *Langmuir* **2007**, *23*, 1388−1393.
(53) Eun, C.; Berkowitz, M. L. Origin of the Hydration Force: Water-Mediated Interaction between Two Hydrophilic Plates. *J. Phys. Chem. B* **2009**, *113*, 13222−13228.
(54) Smirnova, Y.; Aeffner, S.; Risselada, H.; Salditt, T.; Marrink, S.; Müller, M.; Knecht, V. Interbilayer repulsion forces between tension-free lipid bilayers from simulation. *Soft Matter* **2013**, *9*, 10705.
(55) Kanduč, M.; Schlaich, A.; Schneck, E.; Netz, R. R. Hydration repulsion between membranes and polar surfaces: Simulation approaches versus continuum theories. *Adv. Colloid Interface Sci.* **2014**, *208*, 142−152. Special issue in honour of Wolfgang Helfrich.
(56) Schneck, E.; Netz, R. R. From simple surface models to lipid membranes: Universal aspects of the hydration interaction from solvent-explicit simulations. *Curr. Opin. Colloid Interface Sci.* **2011**, *16*, 607−611.
(57) Wynveen, A.; Bresme, F. Interactions of polarizable media in water: A molecular dynamics approach. *J. Chem. Phys.* **2006**, *124*, 104502.
(58) Lu, L.; Berkowitz, M. L. Hydration force between model hydrophilic surfaces: Computer simulations. *J. Chem. Phys.* **2006**, *124*, 101101.
(59) Huang, X.; Zhou, R.; Berne, B. J. Drying and Hydrophobic Collapse of Paraffin Plates. *J. Phys. Chem. B* **2005**, *109*, 3546−3552.
(60) Hua, L.; Zangi, R.; Berne, B. J. Hydrophobic Interactions and Dewetting between Plates with Hydrophobic and Hydrophilic Domains. *J. Phys. Chem. C* **2009**, *113*, 5244−5253.
(61) Eun, C.; Berkowitz, M. L. Thermodynamic and Hydrogen-Bonding Analyses of the Interaction between Model Lipid Bilayers. *J. Phys. Chem. B* **2010**, *114*, 3013−3019.
(62) Hayashi, T.; Pertsin, A. J.; Grunze, M. Grand canonical Monte Carlo simulation of hydration forces between nonorienting and orienting structureless walls. *J. Chem. Phys.* **2002**, *117*, 6271−6280.
(63) Pertsin, A.; Platonov, D.; Grunze, M. Direct computer simulation of water-mediated force between supported phospholipid membranes. *J. Chem. Phys.* **2005**, *122*, 244708.
(64) Schneck, E.; Sedlmeier, F.; Netz, R. R. Hydration repulsion between biomembranes results from an interplay of dehydration and depolarization. *Proc. Natl. Acad. Sci. U. S. A.* **2012**, *109*, 14405−14409.
(65) Kanduč, M.; Schneck, E.; Netz, R. R. Attraction between hydrated hydrophilic surfaces. *Chem. Phys. Lett.* **2014**, *610-611*, 375−380.
(66) Kanduč, M.; Netz, R. R. From hydration repulsion to dry adhesion between asymmetric hydrophilic and hydrophobic surfaces. *Proc. Natl. Acad. Sci. U. S. A.* **2015**, *112*, 12338−12343.
(67) Oostenbrink, C.; Villa, A.; Mark, A. E.; Van Gunsteren, W. F. A biomolecular force field based on the free enthalpy of hydration and solvation: The GROMOS force-field parameter sets 53A5 and 53A6. *J. Comput. Chem.* **2004**, *25*, 1656−1676.
(68) de Gennes, P. G. Wetting: statics and dynamics. *Rev. Mod. Phys.* **1985**, *57*, 827−863.
(69) Bonn, D.; Eggers, J.; Indekeu, J.; Meunier, J.; Rolley, E. Wetting and spreading. *Rev. Mod. Phys.* **2009**, *81*, 739−805.
(70) Grzelak, E. M.; Errington, J. R. Computation of interfacial properties via grand canonical transition matrix Monte Carlo simulation. *J. Chem. Phys.* **2008**, *128*, 014710.
(71) Sendner, C.; Horinek, D.; Bocquet, L.; Netz, R. R. Interfacial Water at Hydrophobic and Hydrophilic Surfaces: Slip, Viscosity, and Diffusion. *Langmuir* **2009**, *25*, 10768−10781.
(72) Bonthuis, D. J.; Gekle, S.; Netz, R. R. Dielectric Profile of Interfacial Water and its Effect on Double-Layer Capacitance. *Phys. Rev. Lett.* **2011**, *107*, 166102.
(73) Godawat, R.; Jamadagni, S. N.; Garde, S. Characterizing hydrophobicity of interfaces by using cavity formation, solute binding, and water correlations. *Proc. Natl. Acad. Sci. U. S. A.* **2009**, *106*, 15119−15124.
(74) Lis, L.; McAlister, M.; Fuller, N.; Rand, R.; Parsegian, V. Interactions between neutral phospholipid bilayer membranes. *Biophys. J.* **1982**, *37*, 657.
(75) LeNeveu, D. M.; Rand, R. P.; Parsegian, V. A. Measurement of forces between lecithin bilayers. *Nature* **1976**, *259*, 601−603.
(76) Attard, P.; N, B.; Mitchell, D. J. The attractive forces between polar lipid bilayers. *Biophys. J.* **1988**, *53*, 457−460.

DOI: 10.1021/acs.langmuir.6b01727
Langmuir 2016, 32, 8767−8782

(77) Kanduč, M.; Schneck, E.; Netz, R. R. Hydration Interaction between Phospholipid Membranes: Insight into Different Measurement Ensembles from Atomistic Molecular Dynamics Simulations. *Langmuir* **2013**, *29*, 9126−9137.
(78) Schneider, M. J. T.; Schneider, A. S. Water in biological membranes: Adsorption isotherms and circular dichroism as a function of hydration. *J. Membr. Biol.* **1972**, *9*, 127−140.
(79) Luzar, A.; Chandler, D. Hydrogen-bond kinetics in liquid water. *Nature* **1996**, *379*, 55−57.
(80) Jones, S.; Thornton, J. M. Principles of protein-protein interactions. *Proc. Natl. Acad. Sci. U. S. A.* **1996**, *93*, 13−20.
(81) Nel, A. E.; Madler, L.; Velegol, D.; Xia, T.; Hoek, E. M. V.; Somasundaran, P.; Klaessig, F.; Castranova, V.; Thompson, M. Understanding biophysicochemical interactions at the nano-bio interface. *Nat. Mater.* **2009**, *8*, 543−557.
(82) Cerdeiriña, C. A.; Debenedetti, P. G.; Rossky, P. J.; Giovambattista, N. Evaporation Length Scales of Confined Water and Some Common Organic Liquids. *J. Phys. Chem. Lett.* **2011**, *2*, 1000−1003.
(83) Sharma, S.; Debenedetti, P. G. Free Energy Barriers to Evaporation ofWater in Hydrophobic Confinement. *J. Phys. Chem. B* **2012**, *116*, 13282−13289.
(84) Setny, P.; Baron, R.; Michael Kekenes-Huskey, P.; McCammon, J. A.; Dzubiella, J. Solvent fluctuations in hydrophobic cavityligand binding kinetics. *Proc. Natl. Acad. Sci. U. S. A.* **2013**, *110*, 1197−1202.
(85) Kanduč, M.; Netz, R. R. Hydration force fluctuations in hydrophilic planar systems. *Biointerphases* **2016**, *11*.01900410.1116/1.4939101
(86) Giovambattista, N.; Rossky, P.; Debenedetti, P. Computational Studies of Pressure, Temperature, and Surface Effects on the Structure and Thermodynamics of Confined Water. *Annu. Rev. Phys. Chem.* **2012**, *63*, 179−200.
(87) Schwierz, N.; Horinek, D.; Netz, R. R. Anionic and Cationic Hofmeister Effects on Hydrophobic and Hydrophilic Surfaces. *Langmuir* **2013**, *29*, 2602−2614. PMID: 23339330.
(88) Jungwirth, P.; Tobias, D. J. Specific Ion Effects at the Air/Water Interface. *Chem. Rev.* **2006**, *106*, 1259−1281.
(89) Otten, D. E.; Shaffer, P. R.; Geissler, P. L.; Saykally, R. J. Elucidating the mechanism of selective ion adsorption to the liquid water surface. *Proc. Natl. Acad. Sci. U. S. A.* **2012**, *109*, 701−705.
(90) Netz, R. R.; Horinek, D. Progress in Modeling of Ion Effects at the Vapor/Water Interface. *Annu. Rev. Phys. Chem.* **2012**, *63*, 401−418.
(91) Pashley, R. Hydration forces between mica surfaces in electrolyte solutions. *Adv. Colloid Interface Sci.* **1982**, *16*, 57−62.
(92) Perkin, S.; Goldberg, R.; Chai, L.; Kampf, N.; Klein, J. Dynamic properties of confined hydration layers. *Faraday Discuss.* **2009**, *141*, 399−413.
(93) Dishon, M.; Zohar, O.; Sivan, U. From Repulsion to Attraction and Back to Repulsion: The Effect of NaCl, KCl, and CsCl on the Force between Silica Surfaces in Aqueous Solution. *Langmuir* **2009**, *25*, 2831−2836.

DOI: 10.1021/acs.langmuir.6b01727
Langmuir 2016, 32, 8767−8782